Heat-transfer rates in equilibrium-wall-modeled LES of supersonic turbulent flows

By X. I. A. Yang, J. Urzay AND P. Moin

1. Motivation and objectives

Wall modeling in large-eddy simulations (WMLES) is of practical relevance for obtaining high-fidelity numerical solutions of engineering flow problems for which an impractically large amount of computational power is required to satisfy the strict near-wall-resolution requirement of a wall-resolved LES (Chapman 1979; Choi & Moin 2012). Most of the earlier work on WMLES has been focused on addressing the momentum transfer near the wall (see reviews by Piomelli & Balaras 2002; Piomelli 2008). In those studies, the emphasis was mostly on low-speed flows, such as incompressible channel flows (Stevens *et al.* 2014; Park & Moin 2016), atmospheric boundary layers (Yang 2016; Jacob & Anderson 2016), urban boundary layers (Bou-Zeid *et al.* 2009; Yang *et al.* 2016) and transitional boundary-layer flows (Sayadi & Moin 2012).

High-speed wall-bounded flows involve a number of additional physical phenomena that complicate the description of the subgrid scales (SGS). For instance, high-speed flows in aero-propulsion applications oftentimes involve the presence of shock waves and intense aerodynamic heating. The former aspect has been thoroughly addressed, for example, by Bermejo-Moreno *et al.* (2014) and Vane *et al.* (2014) in the context of WMLES of supersonic duct flows with adiabatic walls. The results from those studies are fairly realistic, providing wall stresses within less than 15% error. This error is known as the log-layer mismatch and has been discussed in detail in Kawai & Larsson (2012) and Larsson *et al.* (2015). Once this error is removed, the uncertainty in WMLES results reduces to less than 3% (Bou-Zeid *et al.* 2005; Yang *et al.* 2015). It should be noted that the intrinsic coupling between the velocity and thermal fields at high speeds makes necessary the accurate simultaneous prediction of both quantities. Wall modeling for LES of high-speed flows, particularly in situations where there is significant wall heat transfer, remains mostly unexplored in the literature and represents the novel aspect of this report.

In this study, use of the equilibrium wall model is made in LES of high-speed turbulent flows in order to address its capability in predicting wall heat-transfer rates. The flows tested here include supersonic Couette flows and transitional supersonic boundary layers interacting with incident shocks. The results show that the equilibrium wall model performs remarkably well even in situations where aerodynamic heating is most intense in the region near the wall that is not resolved by the LES.

The remainder of this report is organized as follows. The formulation of the equilibrium wall model is summarized in Section 2 for further use throughout the report. The performance of the model is first addressed in Section 3 for WMLES of supersonic Couette flows. The aerothermodynamic effects of a shock wave impinging on a transitional supersonic boundary layer are studied using WMLES in Section 4. Lastly, conclusions are provided in Section 5.

2. Equilibrium wall model

The equilibrium wall model consists of integrating the equations

$$\frac{d}{dy}\left[(\mu+\mu_{t,wm})\,\frac{du_{||}}{dy}\right]=0 \tag{2.1}$$

$$\frac{d}{dy}\left[(\mu+\mu_{t,wm})\,u_{||}\frac{du_{||}}{dy}+c_p\left(\frac{\mu}{\mathrm{Pr}}+\frac{\mu_{t,wm}}{\mathrm{Pr}_{t,wm}}\right)\frac{dT}{dy}\right]=0 \tag{2.2}$$

near the wall (Kawai & Larsson 2010), which represent, respectively, the momentum and total energy conservation equations. In this formulation, y is the wall-normal distance, $u_{||}$ is the velocity component parallel to the wall, T is the static temperature, c_p is the specific heat at constant pressure, μ is the molecular viscosity and Pr is the molecular Prandtl number. Additionally, $\mu_{t,wm}$ is an eddy viscosity given by

$$\mu_{t,wm}=\kappa\rho y\sqrt{\frac{\tau_w}{\rho}}D, \tag{2.3}$$

where $\kappa=0.4$ is the von Kármán constant, ρ is the density and τ_w is the wall shear stress. The eddy viscosity also depends on the wall-normal coordinate through the damping function

$$D=\left[1-\exp\left(-\frac{y^+}{A^+}\right)\right] \tag{2.4}$$

defined in terms of viscous wall units y^+ and the constant $A^+=17$. The symbol $\mathrm{Pr}_{t,wm}=0.9$ corresponds to an eddy Prandtl number.

Equations (2.1)-(2.2) supplemented with (2.3) and (2.4) are numerically integrated in an embedded one-dimensional grid near the wall. Following Kawai & Larsson (2012), the interface between the wall model and the outer LES is located at $h_{wm}=2.5\Delta_y$, which corresponds to the third grid point from the wall in the finite-volume numerical code used here. At the matching location, $y=h_{wm}$, the LES resolved values of temperature $\widetilde{T}$ and velocity $\widetilde{u}_{||}$ are imposed as boundary conditions for the wall model, namely, $u_{||}=\widetilde{u}||$ and $T=\widetilde{T}$. While the no-slip condition $u_{||}=U_w$ is imposed at $y=0$, with U_w the wall velocity for moving walls, the thermal boundary condition there depends on the particular configuration. In this study, both thermal-contact $T=T_w$ and adiabatic $dT/dy|_{y=0}=0$ boundary conditions are used depending on the case, as indicated in Sections 3 and 4, with the wall temperature T_w being assumed to be uniform.

In Eq. (2.2), the first term, which corresponds to a redistribution of total energy by viscous and turbulent stresses, vanishes at the wall. It can be easily decomposed into the sum of the work done by those stresses and a dissipation, the latter given by $(\mu+\mu_{t,wm})(du_{||}/dy)^2$. Near the wall, within the wall-modeled layer, the ratio of the dissipation to the heat flux becomes of order $C_f\mathrm{M}^2$, where C_f is the skin-friction coefficient and M is the Mach number. Since $\mathrm{M}^2\gg 1$ in high-speed flows, aerodynamic heating caused by the viscous dissipation tends to become an important effect near the wall. This heated region, which is located at distances away from the wall that scale with viscous units, is typically not resolved in the outer grid of WMLES, in which the wall-normal grid spacing scales with the local boundary-layer height. Nonetheless, that extra heat has to be transferred to the wall or to the bulk flow in a manner that satisfies the energy balance (2.2). As a result, the aerodynamic heating causes non-monotonicity in the near-wall temperature profile within the wall-modeled region that is correctly captured by the equilibrium wall model, as shown in Sections 3 and 4.

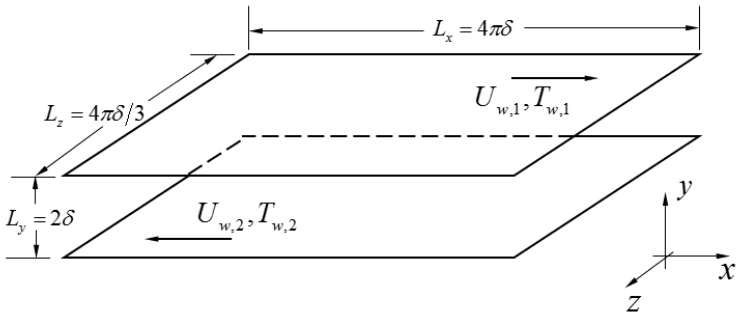

FIGURE 1. Schematics of the computational set-up for WMLES of supersonic Couette flows.

The equilibrium wall model provides the necessary boundary conditions for the integration of the outer LES equations. In particular, the first grid point of the outer LES closest to the wall is fed with the wall shear stress $\tau_w = \mu du_{||}/dy|_{y=0}$ and the wall heat flux $q_w = -(\mu c_p/\mathrm{Pr})dT/dy|_{y=0}$, both being computed from the solution to Eqs. (2.1)-(2.2) supplemented with (2.3) and (2.4). For equilibrium flows, the formulation given above indicates that the momentum flux and the total-energy flux are constant in the log region. As a result,

$$U_w\tau_w - q_w \approx \left(\widetilde{u}_{||}\tau_w + c_p\frac{\mu_{t,\mathrm{LES}}}{\mathrm{Pr}_{t,\mathrm{LES}}}\frac{\partial\widetilde{T}}{\partial y}\right)_{y/\delta\to 0, y^+\gg 1}, \tag{2.5}$$

where $\mu_{t,\mathrm{LES}}$ and $\mathrm{Pr}_{t,\mathrm{LES}}$ are obtained from SGS transport models for the bulk flow. In particular, at high speeds the aerodynamic-heating term $\widetilde{u}_{||}\tau_w$ becomes important and, for instance, makes $\partial\widetilde{T}/\partial y|_{y/\delta\to 0, y^+\gg 1} \neq 0$ in adiabatic conditions $q_w = 0$, since that extra heat must be necessarily dissipated into the bulk flow.

The performance of this equilibrium wall model in computing heat-transfer rates is illustrated in Section 3 in a high-speed Couette flow and in Section 4 in a transitional shock/boundary-layer interaction problem. The numerical code used in this study is the unstructured, finite-volume compressible solver CharLES (Khalighi *et al.* 2011). This code has been extensively used for wall-bounded flow calculations (Larsson *et al.* 2011; Joo *et al.* 2014; Balakumar *et al.* 2014; Canuto & Taira 2015; Bermejo-Moreno *et al.* 2011). Details of this code can be found in Khalighi *et al.* (2011) and the references cited therein. The code solves the Favre-filtered compressible Navier-Stokes equations for the conserved flow quantities of mass, momentum and total energy. In the results presented in Section 3, the eddy viscosity is modeled using the dynamic Vreman model You & Moin (2007), while the dynamic Smagorinsky model (Moin *et al.* 1991) is employed in Section 4 instead. The values of the turbulent Prandtl number and adiabatic coefficient are $\mathrm{Pr}_t = \mathrm{Pr}_{t,\mathrm{LES}} = 0.9$ and $\gamma = 1.4$, respectively. A fourth-order central scheme is used for flux reconstruction in regions away from shocks. Near shocks, which are detected using a Ducros shock sensor (Ducros *et al.* 1999; Bhagatwala & Lele 2009), an essentially non-oscillatory (ENO) scheme is used. A third-order explicit Runge-Kutta scheme is used for time integration. Applications of this code in the context of WMLES can be found, for instance, in Park & Moin (2014).

Case	$N_x \times N_y \times N_z$	$\Delta_x^+ \times \Delta_y^+ \times \Delta_z^+$	B_q	C_f	Re_τ
M3g1	$64 \times 32 \times 32$	$2.6 \times 0.82 \times 1.7(\times 10^2)$	0.13	0.0069	1.3×10^3
M3g2	$128 \times 64 \times 64$	$1.3 \times 0.41 \times 0.86(\times 10^2)$	0.13	0.0069	1.3×10^3
M3g3	$256 \times 128 \times 128$	$0.65 \times 0.21 \times 0.43(\times 10^2)$	0.13	0.0069	1.3×10^3
M6g1	$64 \times 32 \times 32$	$9.3 \times 3.0 \times 6.2(\times 10^2)$	0.35	0.0078	4.4×10^3
M6g2	$128 \times 64 \times 64$	$4.7 \times 1.5 \times 3.1(\times 10^2)$	0.34	0.0078	4.6×10^3
M6g3	$256 \times 128 \times 128$	$2.3 \times 0.74 \times 1.6(\times 10^2)$	0.34	0.0083	4.6×10^3

TABLE 1. WMLES cases for a supersonic Couette flow with equal wall temperatures. The first numerical digit in the case number indicates the Mach number $\mathrm{M} = U_{w,1}/a_{w,1}$ based on the wall velocity and the corresponding speed of sound a_w. The digit Y is an index proportional to the grid size. The Reynolds number Re_τ is based on δ, u_τ, μ_w and ρ_w.

3. WMLES of supersonic Couette flows

In this section, a supersonic flow between two parallel plates, which are moving at the same speed $U_{w,1} = U_{w,2}$ but in opposite directions, is computationally addressed using the set-up sketched in Figure 1. The upper and bottom-wall temperatures are denoted by $T_{w,1}$ and $T_{w,2}$, respectively. A structured Cartesian grid with uniform grid spacing is used that has dimensions $L_x \times L_y \times L_z = 4\pi\delta \times 2\delta \times 4\pi\delta/3$ in the streamwise, wall-normal and spanwise directions, respectively, where δ is half of the channel height. Periodic boundary conditions are imposed in the streamwise and spanwise directions. Statistics are spatially averaged in both x and z directions and temporally averaged for $100t_f$, where $t_f = 2L_x/(U_{w,1} + U_{w,2})$ is the flow-through time. The molecular viscosity in the equilibrium wall model and in the outer LES varies with temperature following the power law $\mu/\mu_{\mathrm{ref}} = (T/T_{\mathrm{ref}})^\sigma$, with $\sigma = 0.7$ and $T_{\mathrm{ref}} = T_{w,1}$.

A number of different WMLES cases are computed that are summarized in Tables 1-3. The cases consider Mach numbers in the range $\mathrm{M} = 3 - 6$ and LES-standard coarse grid sizes ranging from 65K to 4M elements. Emphasis is made on the performance of the equilibrium wall model under different boundary conditions for the temperature.

Six baseline cases (denoted as MXgY in Table 1) are first described that are characterized by having upper and bottom walls at equal temperatures, $T_{w,1} = T_{w,2}$. The digit X is the Mach number $\mathrm{M} = U_{w,1}/a_{w,1}$ based on the wall velocity and the corresponding speed of sound a_w, while the digit Y is an index proportional to the grid size. The Reynolds number, based on δ, $U_{w,1}$, μ_w and the mean (volume-averaged) density ρ_o, is $\mathrm{Re}_\delta = 3.0 \times 10^4$ for the Mach-6 cases and $\mathrm{Re}_\delta = 1.5 \times 10^4$ for the Mach-3 cases, which translate into the friction Reynolds numbers Re_τ values given in Table 1. Although this is not the primary focus of the report, it is worth mentioning that the velocity transformation of Trettel & Larsson (2016) is observed to reasonably collapse the transformed velocities on the incompressible log-law of the wall in the present problem, in which the aerodynamic heating is the sole responsible for the temperature increase since there is no external temperature gradient imposed by the walls. This is shown in Figure 2 for the two cases M3g2 and M6g2 that have intermediate grid resolution.

All the cases with equal wall temperatures lead to monotonic temperature profiles near the wall. This can be observed in Figure 3, which shows the wall-normal profiles of the resulting mean temperatures (up to half of the channel width) for both Mach numbers. Because of the resulting aerodynamic-heating enhancement, the higher the Mach number is, the larger is the bulk-to-wall temperature ratio. However, the bulk-flow temperature appears to be mostly independent of the grid size for the sizes studied here. In contrast,

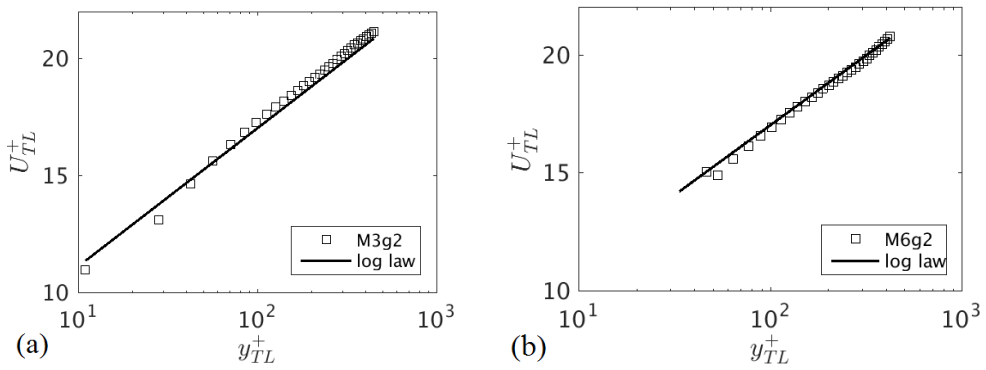

FIGURE 2. TL-transformed velocities in (a) Mach-3 and (b) Mach-6 Couette flows with equal wall temperatures. The log-law velocity profile corresponds to $u^+ = 1/\kappa \log(y^+) + B$, where $B = 5.2$.

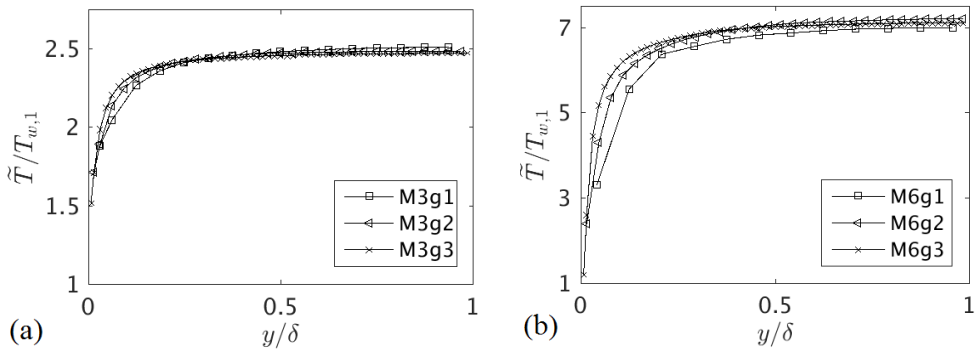

FIGURE 3. Wall-normal profiles of mean temperature for supersonic (a) Mach-3 and (b) Mach-6 Couette flows with equal wall temperatures.

the near-wall temperatures in the coarsest grids (M3g1 and M6g1) are consistently lower than those in the cases where the grid is finer (M3g3 and M6g3). These differences are particularly noticeable at high Mach numbers, as shown in Figure 3(b).

The heat-transfer rate to the wall is represented by the value of the dimensionless parameter

$$B_q = q_w/(\rho_w c_p u_\tau T_w), \tag{3.1}$$

where u_τ is the friction velocity. In Eq. (3.1) the numerator is averaged in time and in the spanwise and streamwise directions. Table 1 shows that B_q increases with the Mach number but is relatively robust to variations in the grid size. Similar observations are made with respect to the skin-friction coefficient

$$C_f = 2\tau_w/(\rho_o U_w^2), \tag{3.2}$$

which does not show a large sensitivity with respect to grid-size variations. The slight differences detected in both C_f and B_q with grid refinement might be ascribed to underperformance of the subgrid-scale model for the dissipation, which stems from Eqs. (2.2) and (2.5).

The two remaining sets of cases analyzed below involve ones in which the near-wall

Case	$N_x \times N_y \times N_z$	$B_{q,1}$	$B_{q,2}$	$C_{f,1}$	$C_{f,2}$
T2g1	$48 \times 24 \times 24$	0.35	0.064	0.0071	0.0071
T2g2	$128 \times 64 \times 64$	0.36	0.065	0.0068	0.0068

TABLE 2. WMLES cases for a supersonic Couette flow with unequal wall temperatures, $T_{w,2} = 9T_{w,1}$. The grid cell aspect ratio is kept the same among all cases.

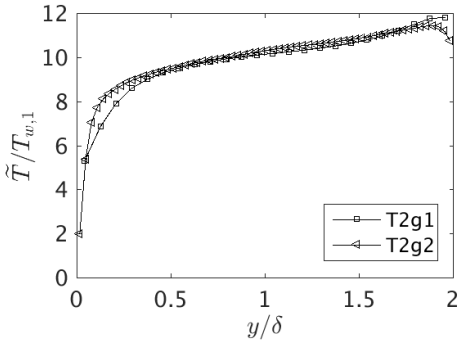

FIGURE 4. Wall-normal profiles of mean temperature for supersonic Couette flows with unequal wall temperatures, $T_{w,2} = 9T_{w,1}$. Triangles and circles indicate results for coarse and fine grids, respectively.

temperatures are non-monotonic. Consider first the cases T2gY outlined in Table 2, in which the wall temperatures are such that $T_{w,2} = 9T_{w,1}$ for two different grids of varying size. The wall translational velocities are $U_{w,1} = U_{w,2} = 6c_{w,1}$. Compared to the cases with equal wall temperature in Table 1, increasing the top-wall temperature does not have a strong effect on the skin-friction coefficient. In contrast, the heat-transfer rate on the top wall, $B_{q,2}$ is largely decreased by the increase in the temperature.

As the top-wall temperature is increased, the peak temperature caused by the aerodynamic heating moves increasingly towards the top wall. If the top-wall temperature is increased to very high values, the peak temperature is reached at the top wall. At the intermediate top-wall temperature analyzed here, $T_{w,2} = 9T_{w,1}$, the fine-grid case (T2g2) shown in Figure 4 captures the temperature peak near the top wall caused by the aerodynamic heating. However, in the computation performed with the coarse grid (T2g1), the peak ceases to be detected in the resolved temperature profile, as observed in Figure 4. Despite this apparent shortfall, the heat-transfer rate predicted by the equilibrium wall model in the coarse-grid calculation (T2g1) is very similar to the one obtained using the fine grid (T2g2), as indicated by the resulting values of $B_{q,2}$ in Table 2. The reason for this is that the aerodynamic heating has been correctly accounted for in the computation of the near-wall temperature using the matching condition Eq. (2.5).

The effect of adiabatic boundary conditions is addressed in the last set of cases AdgY in Table 3, in which $U_{w,1} = U_{w,2} = 3a_{w,1}$ and the top wall is adiabatic, $dT/dy|_{w,2} = 0$. Figure 5 shows the resulting profiles of resolved temperature, which is maximum at the top wall. Because of the reasons explained in Section 2 within the context of Eq. (2.5), The temperature does not necessarily have to arrive with zero slope at the adiabatic wall. Conversely, the temperature slope increasingly departs from zero as the grid is coarsened, which finds justification in the fact that the aerodynamic heat generated in the near-wall region, which is computed by the equilibrium wall model, must be transferred into the

Case	$N_x \times N_y \times N_z$	$B_{q,1}$	$B_{q,2}$	$C_{f,1}$	$C_{f,2}$
Adg1	$64 \times 32 \times 32$	0.18	0.0	0.0065	0.0065
Adg2	$128 \times 64 \times 64$	0.18	0.0	0.0069	0.0069

TABLE 3. WMLES cases for a supersonic Couette flow with upper adiabatic wall, $dT/dy|_{w,2} = 0$. The grid cell aspect ratio is kept the same among all cases.

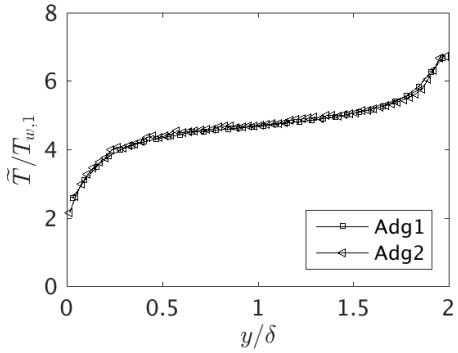

FIGURE 5. Wall-normal profiles of mean temperature for supersonic Couette flows with upper adiabatic wall, $dT/dy|_{w,2} = 0$. Triangles and circles indicate results for coarse and fine grids, respectively

bulk flow if the wall is adiabatic. The adiabatic boundary condition is strictly satisfied on the physical wall, in the form of a zero gradient of the temperature computed from Eq. (2.2) within the wall-modeled region. Therefore, the resulting wall heat-transfer rates reported in Table 3 become mostly insensitive to the tested resolutions and to the presence or absence of adiabaticity in the resolved temperature field. It is worth mentioning that, in low-speed flows, the effect of the aerodynamic heating is negligible and the equilibrium wall model simplifies and correctly predicts a fully adiabatic resolved temperature field.

4. WMLES of shock-wave interactions with transitional boundary layers

In this last part of the report, the performance of the equilibrium wall model described in Section 2 is tested against DNS and experimental data in a transitional supersonic boundary layer interacting with an incident shock wave. The corresponding computational set-up is sketched in Figure 6. The size of the computational domain is $L_x \times L_y \times L_z = 300 \times 25 \times 45$ in units of the displacement thickness $\delta_o^\star$, and the grid size is $N_x \times N_y \times N_z = 256 \times 64 \times 72$ ($\approx$ 1M cells). This grid size is in contrast with that of the DNS performed by Sandham *et al.* (2014), which has approximately 200M cells. Those DNS results, along with the experiments of Willems *et al.* (2015) and Schülein & Wagner (2012) in the same configuration, will be used below for comparisons.

The boundary conditions used in the WMLES are as follows. Periodicity is imposed in the spanwise directions, while a similarity solution for compressible laminar boundary layers is imposed at the inflow (see White & Corfield (2006) for details). The inflow free-stream Mach number is 6. The inflow displacement thickness of the boundary layer, the free-stream speed of sound, the free-stream density (ρ_∞), and the free-stream temperature (T_∞) are taken as reference values to normalize lengths, velocities, densities and temperatures. The resulting inflow Reynolds number is 6830. In

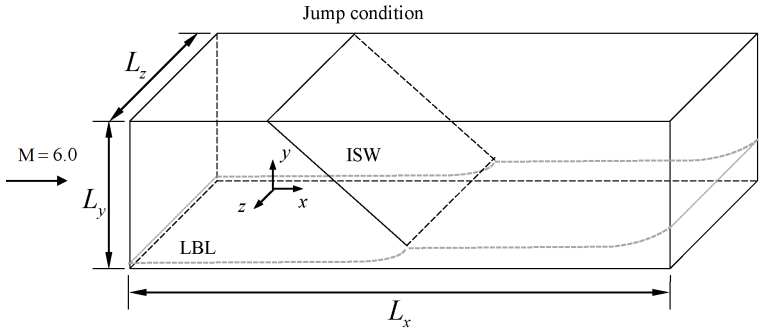

FIGURE 6. Schematics of the computational set-up for WMLES of shock-induced heating in transitional supersonic boundary layers (ISW: incident shock wave; LBL: laminar boundary layer).

the present flow regime, the sole action of the shock is unable to cause transition. In order to trigger transition, the forcing method of Sandham *et al.* (2014) is followed, by which broadband acoustic disturbances are added to the inflow density as $\rho' = AW(y)\sum_{j=0}^{J}\cos(2\pi jz/L_z+\phi_j)\sum_{k=1}^{K}\sin(2\pi f_k t+\psi_k)$, where ϕ_j and ψ_k are random phases, $f = 0.02$ is the frequency, and $J = 16$ and $K = 20$ are cutoff wavenumbers. Additionally, $W(y) = 1 - e^{-y^3}$ is a window function that dampens the disturbances within the boundary layer. The amplitude A of the disturbance is adjusted to provide an equivalent 0.28% root-mean-square disturbance to the free-stream streamwise velocity at the transition location.

The bottom-wall temperature is kept constant at $T_w = 4.5$. The velocity, density and temperature at the top boundary upstream from the shock are set to the reference values $U_\infty = 6$, $\rho_\infty = 1$, and $T_\infty = 1$. Rankine-Hugoniot jump conditions are used downstream from the shock to obtain the corresponding boundary values necessary for an obliquely impinging shock wave arising from a 4° wedge. A characteristic Navier-Stokes boundary condition is superimposed there to warrant non-reflectivity of pressure waves. The shock-impingement location computed from the inviscid wave propagation is at $x = 150$, which translates into a local Reynolds number $\mathrm{Re}_x = 1.34\times10^6$. A non-reflecting sponge layer of thickness $\delta x = 15$ is placed near the outflow. The molecular viscosity in the equilibrium wall model and in the outer LES varies with temperature according to the Sutherland's law

$$\frac{\mu}{\mu_{\mathrm{ref}}} = \left(\frac{T}{T_{\mathrm{ref}}}\right)^{1.5}\frac{T_{\mathrm{ref}}+S}{T+S}, \tag{4.1}$$

where $S/T_{\mathrm{ref}} = 1.69$ is a constant and T_{ref} is set equal to the free-stream temperature.

Instantaneous contours of the spanwise-averaged magnitude of the resolved density gradient are shown in Figure 7. The incident shock creates a local recirculation in the interaction zone as a result of the induced adverse pressure gradient. The shock reflects into the form of an expansion fan along with weak compression waves. The boundary layer rapidly undergoes transition downstream from the interaction region. The transition is clearly visible in the velocity isocontours shown in Figure 8(a). Specifically, velocity streaks form that may be enhanced by Görtler-like instabilities engendered by the concave curvature of the streamlines on the edge of the boundary layer downstream from the interaction zone. These transition dynamics are accompanied with a large increase in the flow temperature, observed in Figure 8(b). Correspondingly, the dimensionless wall

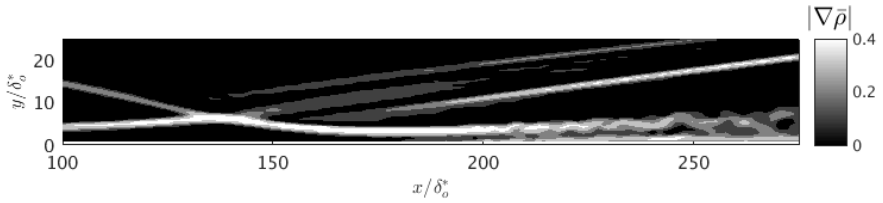

FIGURE 7. Instantaneous isocontours of the spanwise-averaged magnitude of the resolved density gradient.

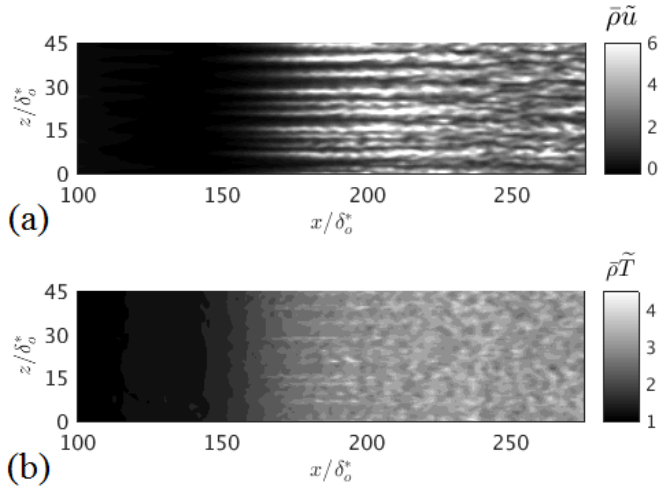

FIGURE 8. Instantaneous isocontours of (a) $\overline{\rho}\widetilde{u}$ and (b) $\overline{\rho}\widetilde{T}$, both being extracted at a distance $y = 0.4$, which corresponds to the third LES-grid point away from the wall.

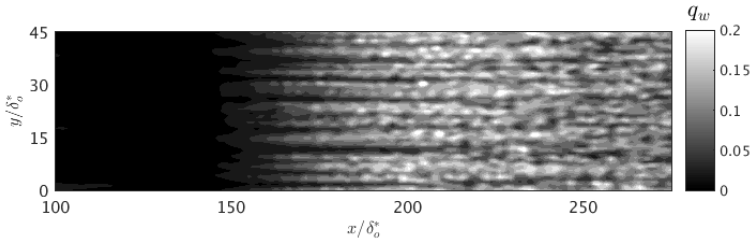

FIGURE 9. Instantaneous isoontours of the wall heat-transfer rate predicted by the equilibrium wall model.

heat-transfer rate q_w shown in Figure 9 undergoes a large increase upon transition. Remarkably, footprints of the velocity streaks are clearly discerned in the instantaneous wall heat transfer that highlight the importance of the near-wall momentum transport captured by the equilibrium wall-model.

A more quantitative assessment of the wall heat-transfer rate is made in Figure 10 in terms of the Stanton number

$$\mathrm{St} = q_w/[\rho_\infty U_\infty c_p(T_r - T_w)], \tag{4.2}$$

where $T_r = T_\infty[1+r(\gamma-1)M_\infty^2/2]$ is the recovery temperature and $r = \mathrm{Pr}^{1/2}$ is the recov-

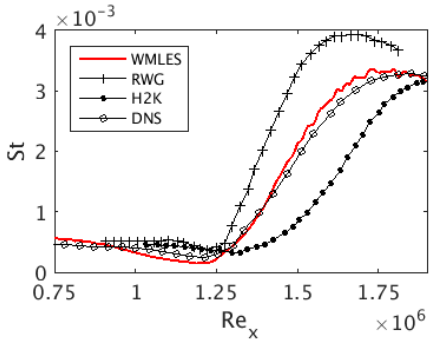

FIGURE 10. Comparison of Stanton numbers predicted by the WMLES using the equilibrium wall model, by experiments (RWG and H2K) from Willems *et al.* (2015) and Schülein & Wagner (2012), and by DNS from Sandham *et al.* (2014).

ery factor. In Eq. (4.2), the numerator is averaged in both time and spanwise direction. Note that the resolved temperature is not significantly larger than the wall temperature anywhere in the LES grid. In particular, the near-wall peak in the static temperature is not resolved since the coarse LES grid could not resolve the strong dissipation near the wall. However, it is modeled by the equilibrium wall model. As a result, the equilibrium-wall-modeled LES reproduces well the DNS results by Sandham *et al.* (2014). Similarly to DNS, the WMLES follows reasonably -but does not match- the experimental results of Willems *et al.* (2015) and Schülein & Wagner (2012) since these use different levels of free-stream turbulence that are difficult to univocally characterize in a boundary-layer transition problem.

In conclusion, Figure 10 shows that the equilibrium wall model provides an excellent prediction of the DNS results at a much lower computational cost. However, additional aspects require future research in order to make the model fully predictive in transition problems. These include the treatment of the growth of the intrinsic instabilities upstream from the shock in a coarse grid. A report published in this same volume provides preliminary methodologies to solve this issue in low-speed flows (Lozano-Durán *et al.* 2011).

5. Conclusions

In this work, the equilibrium wall model is investigated within the context of high-speed flows where aerodynamic heating becomes an important effect in quantifying wall heat-transfer rates. The formulation of the model is described making emphasis on heat-transfer aspects. Focus is made on two different configurations: supersonic Couette flows, and shock-induced heating in transitional supersonic boundary layers. Since the distance from the wall to the spatial location of the maximum of the aerodynamic-heating rate scales with inner viscous units, typical LES grids, whose resolution in the wall-normal direction scales with outer units, tend to miss the corresponding temperature peak. However, in coarse LES grids, the equilibrium wall model is able to account for subgrid-scale aerodynamic heating and provides predictions of wall heat-transfer rates that are indistinguishable from those in finer LES grids, in which the near-wall resolution is sufficient to resolve the aerodynamic heating. In particular, the equilibrium wall model correctly predicts the wall heat-transfer rate since the appropriate matching condition with the outer LES is employed.

The performance of the equilibrium wall model is studied in supersonic Couette flows, where consistent predictions of wall heat-transfer rates and wall shear stresses are obtained in grids which are vastly different in size, and in computational set-ups subject to different thermal boundary conditions. Similarly, the model is able to reproduce the DNS wall heat-transfer rate in the problem of a shock impinging on a transitional supersonic boundary layer. Despite the presence of flow separation and a strong adverse pressure gradient, realistic predictions on the mean wall heat-transfer rate are found in the present WMLES calculation that uses merely 1M cells. These considerations highlight the importance of correctly capturing the subgrid-scale aerodynamic heating in WMLES.

In summary, it is concluded that the equilibrium wall model performs correctly for the high speed flows analyzed here. Realistic predictions of higher-order statistics might require non-equilibrium wall-model effects to be included (Park & Moin 2014; Yang *et al.* 2015), but these are beyond the scope of this investigation. Similarly, there are several other wall-modeling aspects that influence the heat-transfer rates and remain largely unexplored in WMLES of high-speed aerothermodynamics, such as non-equilibrium gas-dynamic effects in energy transfer and near-wall chemical reactions, including ionization, ablation and dissociation-recombination processes, but these are deferred to future work.

Acknowledgments

This investigation was funded by the US AFOSR, Grant #1194592-1-TAAHO.

REFERENCES

Balakumar, P., Park, G. & Pierce, B. 2014 DNS, LES, and wall-modeled LES of separating flow over periodic hills. *Proceedings of the Summer Program*, Center for Turbulence Research, Stanford University, pp. 407–415.

Bermejo-Moreno, I., Campo, L., Larsson, J., Bodart, J., Helmer, D. & Eaton, J. K. 2014 Confinement effects in shock wave/turbulent boundary layer interactions through wall-modeled large-eddy simulations. *J. Fluid Mech.* **758**, 5–62.

Bermejo-Moreno, I., Larsson, J., Campo, L., Bodart, J., Vicquelin, R., Helmer, D. & Eaton, J. 2011 Wall-modeled large-eddy-simulation of shock/turbulent boundary-layer interaction in a duct. *Annual Research Briefs,* Center for Turbulence Research, Stanford University, pp. 49–62.

Bhagatwala, A. & Lele, S. K. 2009 A modified artificial viscosity approach for compressible turbulence simulations. *J. Comput. Phys.* **228**, 4965–4969.

Bou-Zeid, E., Meneveau, C. & Parlange, M. 2005 A scale-dependent lagrangian dynamic model for large eddy simulation of complex turbulent flows. *Phys. Fluids* **17**, 025105.

Bou-Zeid, E., Overney, J., Rogers, B. D. & Parlange, M. B. 2009 The effects of building representation and clustering in large-eddy simulations of flows in urban canopies. *Bound.-Lay. Meteorol.* **132**, 415–436.

Canuto, D. & Taira, K. 2015 Two-dimensional compressible viscous flow around a circular cylinder. *J. Fluid Mech.* **785**, 349–371.

Chapman, D. R. 1979 Computational aerodynamics development and outlook. *AIAA J.* **17**, 1293–1313.

Choi, H. & Moin, P. 2012 Grid-point requirements for large eddy simulation: Chapman's estimates revisited. *Phys. Fluids* **24**, 011702.

Ducros, F., Ferrand, V., Nicoud, F., Weber, C., Darracq, D., Gacherieu, C. & Poinsot, T. 1999 Large-eddy simulation of the shock/turbulence interaction. *J. Comput. Phys.* **152**, 517–549.

Jacob, C. & Anderson, W. 2016 Conditionally averaged large-scale motions in the neutral atmospheric boundary layer: Insights for aeolian processes. *Bound.-Lay. Meteorol.* (In Press), doi:10.1007/s10546-016-0183-4.

Joo, J., Medic, G., Philips, D. & Bose, S. 2014 Large-eddy simulation of a compressor rotor. *Proceedings of the Summer Program*, Center for Turbulence Research, Stanford University, p. 467.

Kawai, S. & Larsson, J. 2010 A dynamic wall model for large-eddy simulation of high Reynolds number compressible flows. *Annual Research Briefs*, Center for Turbulence Research, Stanford University, pp. 25–37.

Kawai, S. & Larsson, J. 2012 Wall-modeling in large eddy simulation: Length scales, grid resolution, and accuracy. *Phys. Fluids* **24**, 015105.

Khalighi, Y., Nichols, J. W., Lele, S., Ham, F. & Moin, P. 2011 Unstructured large eddy simulation for prediction of noise issued from turbulent jets in various configurations. *AIAA Paper* 2011-2886.

de Lageneste, L. D. & Pitsch, H. 2001 Progress in large-eddy simulation of premixed and partially-premixed turbulent combustion. *Annual Research Briefs*, Center for Turbulence Research, Stanford University, pp. 97–107.

Larsson, J., Kawai, S., Bodart, J. & Bermejo-Moreno, I. 2015 Large eddy simulation with modeled wall-stress: recent progress and future directions. *Mechanical Engineering Reviews* **1**, 1–23.

Larsson, J., Vicquelin, R. & Bermejo-Moreno, I. 2011 Large eddy simulations of the hyshot ii scramjet. *Annual Research Briefs*, Center for Turbulence Research, Stanford University, pp. 63–74.

Lozano-Durán, A., Hack, M. J. P., Park, G. I. & Moin, P. 2016 Modeling boundary-layer transition in DNS and LES using parabolized stability equations. *Annual Research Briefs*, Center for Turbulence Research, Stanford University, pp. 29–37.

Moin, P., Squires, K., Cabot, W. H. & Lee, S. 1991 A dynamic subgridscale model for compressible turbulence and scalar transport. *Phys. Fluids* **3**, 2746–2757.

Park, G. I. & Moin, P. 2014 An improved dynamic non-equilibrium wall-model for large eddy simulation. *Phys. Fluids* **26**, 015108.

Park, G. I. & Moin, P. 2016 Space-time characteristics of wall-pressure and wall shear-stress fluctuations in wall-modeled large eddy simulation. *Phys. Rev. Fluids* **1**, 024404.

Piomelli, U. 2008 Wall-layer models for large-eddy simulations. *Prog. Aerosp. Sci.* **44**, 437–446.

Piomelli, U. & Balaras, E. 2002 Wall-layer models for large-eddy simulations. *Annu. Rev. Fluid Mech.* **34**, 349–374.

Sandham, N., Schülein, E., Wagner, A., Willems, S. & Steelant, J. 2014 Transitional shock-wave/boundary-layer interactions in hypersonic flow. *J. Fluid Mech.* **752**, 349–382.

Sayadi, T. & Moin, P. 2012 Large eddy simulation of controlled transition to turbulence. *Phys. Fluids* **24**, 114103.

Schülein, E. & Wagner, A. 2012 *Ludwieg-tube experiments on the effects of laminar-*

turbulent transition on the SWBLI at Mach 6, In ESA-TRP *Laminar to Turbulent Transition in Hypersonic Flows*, TN 4110. Tech. Rep. DLR-IB 224?2011 A 64, German Aerospace Center, Göttingen.

Stevens, R. J., Wilczek, M. & Meneveau, C. 2014 Large-eddy simulation study of the logarithmic law for second-and higher-order moments in turbulent wall-bounded flow. *J. Fluid Mech.* **757**, 888–907.

Trettel, A. & Larsson, J. 2016 Mean velocity scaling for compressible wall turbulence with heat transfer. *Phys. Fluids* **28**, 026102.

Vane, Z., Bermejo-Moreno, I. & Lele, S. K. 2014 Wall-modeled large-eddy simulations of a supersonic turbulent flow in a square duct. *AIAA Paper* 2014-2209.

White, F. M. & Corfield, I. 2006 *Viscous Fluid Flow*. McGraw-Hill New York.

Willems, S., Gülhan, A. & Steelant, J. 2015 Experiments on the effect of laminar–turbulent transition on the SWBLI in H2K at mach 6. *Experiments in Fluids* **56**, 1–19.

Yang, X., Sadique, J., Mittal, R. & Meneveau, C. 2015 Integral wall model for large eddy simulations of wall-bounded turbulent flows. *Phys. Fluids* **27**, 025112.

Yang, X. I. 2016 On the mean flow behaviour in the presence of regional-scale surface roughness heterogeneity. *Bound.-Lay. Meteorol.* pp. 1–17.

Yang, X. I., Sadique, J., Mittal, R. & Meneveau, C. 2016 Exponential roughness layer and analytical model for turbulent boundary layer flow over rectangular-prism roughness elements. *J. Fluid Mech.* **789**, 127–165.

You, D. & Moin, P. 2007 A dynamic global-coefficient subgrid-scale eddy-viscosity model for large-eddy simulation in complex geometries. *Phys. Fluids* **19**, 065110.